SPECIAL FEATURE

Rayleigh–Taylor instabilities in high-energy density settings on the National Ignition Facility

Bruce A. Remington[a,1,2], Hye-Sook Park[a,1], Daniel T. Casey[a,1], Robert M. Cavallo[a], Daniel S. Clark[a], Channing M. Huntington[a], Carolyn C. Kuranz[b], Aaron R. Miles[a], Sabrina R. Nagel[a], Kumar S. Raman[a], and Vladimir A. Smalyuk[a]

[a]Lawrence Livermore National Laboratory, Livermore, CA 94550; and [b]Atmospheric, Oceanic, Space Science Department, University of Michigan, Ann Arbor, MI 48105

Edited by William A. Goddard III, California Institute of Technology, Pasadena, CA, and approved May 10, 2018 (received for review September 30, 2017)

The Rayleigh–Taylor (RT) instability occurs at an interface between two fluids of differing density during an acceleration. These instabilities can occur in very diverse settings, from inertial confinement fusion (ICF) implosions over spatial scales of $\sim 10^{-3}$–10^{-1} cm (10–1,000 μm) to supernova explosions at spatial scales of $\sim 10^{12}$ cm and larger. We describe experiments and techniques for reducing ("stabilizing") RT growth in high-energy density (HED) settings on the National Ignition Facility (NIF) at Lawrence Livermore National Laboratory. Three unique regimes of stabilization are described: (*i*) at an ablation front, (*ii*) behind a radiative shock, and (*iii*) due to material strength. For comparison, we also show results from nonstabilized "classical" RT instability evolution in HED regimes on the NIF. Examples from experiments on the NIF in each regime are given. These phenomena also occur in several astrophysical scenarios and planetary science [Drake R (2005) *Plasma Phys Controlled Fusion* 47:B419–B440; Dahl TW, Stevenson DJ (2010) *Earth Planet Sci Lett* 295:177–186].

Rayleigh–Taylor instability | high-energy density experiments | National Ignition Facility

High-energy density (HED) experiments, typically defined as experiments requiring energy densities $> \sim 10^{12}$ erg/cm^3 or pressures $> \sim 100$ GPa to be possible, offer unique opportunities to study phenomena that typically can be found only in high-energy astrophysics and astronomy. Examples include the study of the properties of stellar and planetary interiors (3, 4), stellar and planetary formation dynamics (5, 6), stellar explosions (supernovas) (7, 8), gamma-ray bursts (9), galactic mergers (10), and inertial confinement fusion (ICF) implosions (11–13). Aspects of these phenomena can be accessed in the laboratory using high-energy, high-power lasers, such as the National Ignition Facility (NIF) laser at Lawrence Livermore National Laboratory (LLNL) (14, 15) and the Omega laser (16) at the University of Rochester. An example of ICF research on the NIF is illustrated in Fig. 1*A*, which shows results from a 3D simulation of an ICF implosion (13). The red region in the center of the image on the left is the central hot spot just before the time of peak nuclear yield ("bang time"). The predicted peak temperature in the hot spot is 3–4 keV. Fig. 1*B* shows output from the same 3D simulation, but 170 ps later, at bang time. Note now that the hot spot is cooler, due to mixing of shell material into the deuterium–tritium (DT) hot spot and conductive losses, but is considerably denser, having reached peak convergence (13). Fig. 1*C* shows experimentally measured neutron yields from an extensive series of cryogenic layered DT capsule implosions on the NIF, at four different peak laser powers (17). The results are plotted as a function of experimentally inferred mix mass, that is, the amount of CH(Si) capsule shell material that is mixed deep enough into the central hot spot that it radiates in the soft X-ray regime, enhancing the observed X-ray emission, cooling the hot spot, and lowering the nuclear yield. When the mix mass into the hot spot exceeds ~100 ng, the nuclear yield drops by an order of magnitude or more. The results shown in Fig. 1*D* are similar to Fig. 1*C* except that the horizontal axis corresponds to the X-ray enhancement factor, that is, the increase in X-ray emission over what is expected from an unmixed ("clean") hot spot (17). In Fig. 1*D*, the blue symbols correspond to the low-adiabat, high-compression four-shock "low-foot" drive, whereas the green symbols correspond to the "high-foot" higher-adiabat three-shock drive, which reduces the hot-spot mix mass considerably, albeit at lower fuel areal density (17).

Two of the dominant sources of this hot-spot mix are ablation-front Rayleigh–Taylor (RT) and Richtmyer–Meshkov (RM) instabilities, which amplify preexisting defects and other perturbations. Predictions of RT growth and its effects in ICF and HED experiments use large-scale 2D and 3D radiation hydrodynamics simulations, which can also include models of material strength, which can act like an effective lattice viscosity. For HED plasmas, assuming that viscosity and surface tension are negligible, we can write a simple heuristic equation to approximate linear regime, ablation-front RT growth rate, γ_{RT}, namely

$$\gamma_{RT} = \alpha \left[\frac{Akg}{1+kL} \right]^{\frac{1}{2}} - \beta k v_a, \qquad [1]$$

whereby perturbations of initial amplitude η_0 grow as $\eta = \eta_0\, e^{\gamma t}$, provided $\eta/\lambda \ll 0.1$ (18–33). Here α and β are fitting parameters, $k = 2\pi/\lambda$ is the perturbation wave number, g is the acceleration of the RT unstable interface, $L = \rho/(\nabla\rho)$ is the density gradient scale length at the ablation front, $v_a = (dm_a/dt)/\rho_{max}$

Significance

We present research results on the Rayleigh–Taylor (RT) instability at an unstable interface under high-energy density conditions using the National Ignition Facility at Lawrence Livermore National Laboratory. We can reach pressures in the 100-TPa regime on the Hugoniot, or ~500-GPa regime along a quasi-isentrope, allowing the sample under study to remain solid, at planetary interior pressures. We observe RT stabilization (*i*) at an ablation front; (*ii*) in the presence of a strongly radiative shock; and (*iii*) in a unique regime of quasi-isentropic, high pressure, solid-state material flow, where the material strength significantly affects the evolution of a hydrodynamically unstable interface.

Author contributions: H.-S.P., R.M.C., D.S.C., A.R.M., and K.S.R. designed research; B.A.R., H.-S.P., D.T.C., C.M.H., C.C.K., S.R.N., and V.A.S. performed research; H.-S.P., D.T.C., and K.S.R. contributed new experimental and simulation tools; H.-S.P., D.T.C., C.M.H., and S.R.N. analyzed data; and B.A.R., H.-S.P., D.T.C., and D.S.C. wrote the paper.

The authors declare no conflict of interest.

This article is a PNAS Direct Submission.

[1]B.A.R., H.-S.P., and D.T.C. contributed equally to this work.

[2]To whom correspondence should be addressed. Email: remington2@llnl.gov.

Published online June 26, 2018.

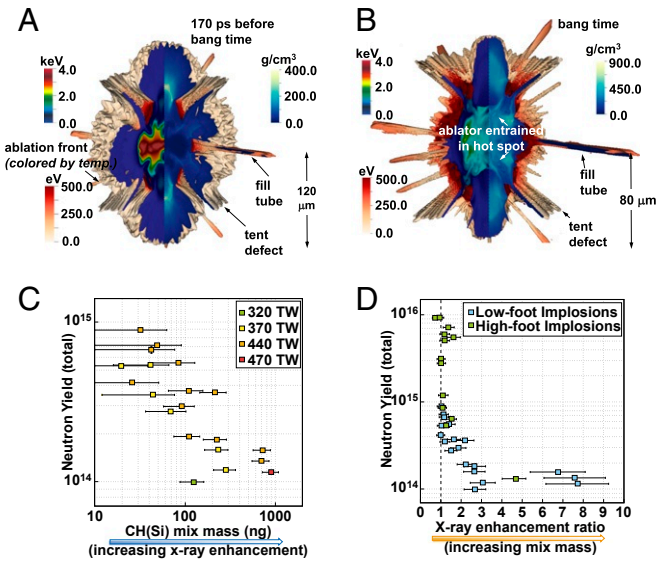

Fig. 1. Results from ICF research on the NIF laser facility. (*A*) A result from a 3D implosion simulation for the low-adiabat, four-shock low-foot drive of a NIF capsule implosion at 170 ps before bang time (i.e., the time of peak nuclear yield), for NIF shot N120405. *Upper Right* color scale represents density (grams per cubic centimeter), and *Upper Left* color scale indicates hot spot ion temperature in kiloelectronvolts. Note that the peak temperature in the hot spot is ∼3–4 keV. *Lower Left* color scale corresponds to electron temperature in electronvolts at the ablation front, and the spatial scale corresponding to 120 μm is indicated by the arrow on the lower right side (13). (*B*) Similar to *A* except at bang time (the moment of peak nuclear yield). Note that the hot-spot peak temperature is slightly lower than in *A* but the peak density is significantly higher (13). (*C*) Experimental results of total neutron yield vs. hot-spot mix mass (nanograms) from a set of cryogenic layered DT implosions on the NIF, showing the monotonic decrease in yield as mix mass increases (17). The different-colored symbols correspond to different peak powers in terawatts (TW) of the NIF drive laser. (*D*) Similar to *C* except the horizontal axis corresponds to the X-ray enhancement factor, which is proportional to increasing mix mass (main text). Here, the blue symbols correspond to the low-adiabat four-shock drive, whereas the green symbols correspond to the high-foot higher-adiabat three-shock drive, which reduces the hot-spot mix mass considerably, albeit at lower fuel areal density (17). (*A* and *B*) Reproduced from ref. 13, with permission of AIP Publishing. (*C* and *D*) Reproduced from ref. 17, with permission of AIP Publishing.

is the ablation velocity, and m_a is areal mass density (g/cm^2). This equation is only approximate, but does illustrate that the RT growth rate, γ_{RT}, decreases as v_a and L increase. Defining the classical RT growth rate as classical $\gamma_{classical} = (Akg)^{1/2}$, it is generally the case that ablation-front RT growth is reduced from classical, $\gamma_{RT} < \gamma_{classical}$, an effect which is typically referred to as "ablative stabilization." There is an ongoing effort at the NIF to understand and control ablation-front RT growth and hot-spot mix, for the various drive pulse shapes (laser power vs. time) that are used in ICF and HED research (13, 17, 34–37). Typical pressures at the ablation front on the NIF can range from ∼1 TPa to 10 TPa or higher. At peak compression in the hot spot, these pressures can be amplified to 1–10 PPa by shock heating and spherical convergence (38).

In the following, we present four areas of HED research on the NIF: (*i*) ablatively stabilized, spherically converging hydrodynamic instability experiments, measuring RT growth factor vs. perturbation mode number; (*ii*) a set of planar embedded interface, "classical" (nonstabilized) hydrodynamic instability experiments; (*iii*) radiative shock stabilized, hydrodynamic instability results in planar geometry; and (*iv*) a material strength stabilized hydrodynamic instability experiment. We then summarize and conclude.

Ablation Front, Spherical Hydrodynamic Instability Experiments

A wide variety of experiments are being performed on the NIF to study the hydrodynamics of ICF capsule implosions (17, 35–45). At the ablation front, instability growth of preimposed modulations was measured with in-flight, time-resolved, face-on, X-ray radiography (35, 36, 39, 46, 47). Perturbation growth of "native roughness" modulations and engineering features such as fill tubes and capsule support membranes was also measured (37, 42, 48), as was instability growth at the ablator–ice interface (41). In the deceleration phase of implosions, RT growth from low-mode asymmetries and high-mode perturbations was measured near peak compression with X-ray and nuclear techniques. In one technique, the self-emission from the hot spot was enhanced with 1% argon dopant to "self-backlight" the shell in flight (40), and "adiabat-shaping" techniques were developed (49) to control hot-spot mix in cryogenic layered DT implosions (36, 50, 51).

We show in Fig. 2*A* the experimental configuration where a hollow Au cylindrical cavity ("hohlraum") is irradiated on the inside by 192 NIF laser beams, generating an ∼250- to 300-eV

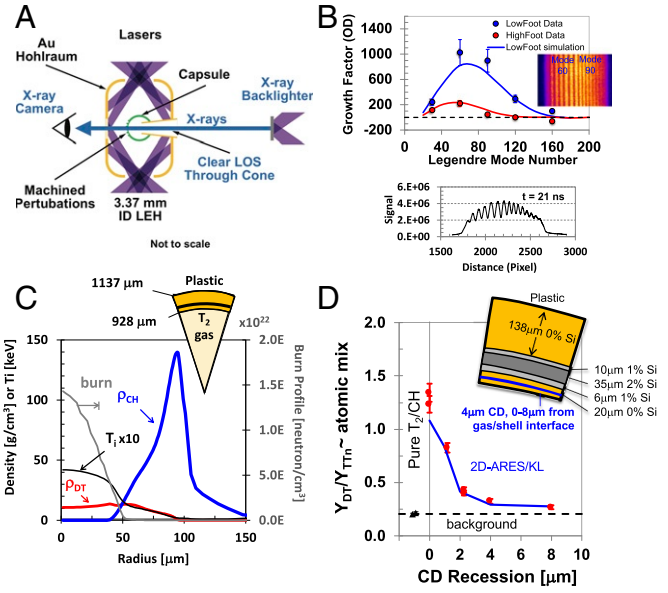

Fig. 2. Results from mix experiments and simulations on the NIF (17, 37). (*A*) The experimental configuration for an inflight radiography capsule implosion experiment on the NIF, showing the capsule, the hohlraum radiation cavity, the face-on backlighter, and a subset of the lasers used. (*B*) Simulated vs. experimentally measured ablation front perturbation growth factor as a function of perturbation Legendre mode number at a convergence ratio of $R_0/R \sim 2$, based on inflight radiography measurements, for the low-entropy, high-compression low-foot drive (blue curve) and the higher-entropy, lower-compression high-foot drive (red curve) (35, 45). The blue and red symbols with error bars are the corresponding experimental data points. (*C*) The predicted results from simulations of shell density (blue curve labeled ρCH, grams per cubic centimeter), hot-spot density labeled ρDT (red, grams per cubic centimeter), hot-spot ion temperature labeled $T_i \times 10$ (black, keV), and hot-spot burn profile labeled "burn" (gray, neutrons per cubic centimeter) for the experiment shown in *A*. Values from the $T_i \times 10$ black curve need to be divided by 10 to give the predicted result. The peak hot-spot ion temperature at this time shown is slightly over 4 keV. (*D*) Experimentally observed DT yield of 14-MeV neutrons vs. recession distance (in micrometers) of a CD marker layer from the shell–hot-spot interface for a series of T_2 gas-filled capsule implosions on the NIF laser. *Insets* in *C* and *D* show a sketch of the T_2 gas-filled capsule used in these experiments (17). (*B*) Reprinted with permission from ref. 35. Copyright (2014) by the American Physical Society. (*C* and *D*) *Insets* reproduced from ref. 43, with permission of AIP Publishing.

radiation drive for the "hydro-growth radiography" (HGR) platform (35, 45). This radiation drive ablatively implodes a hollow spherical capsule of 1-mm initial radius and 150–200 μm initial shell thickness, which consists of doped and undoped layers of plastic. Various dopant layers, such as CH(I), CH(Ge), and CH(Si), are used to block hard X-ray preheat generated at the ablation front. An example inflight X-ray radiograph from a preimposed ripple pattern on the ablation front of an imploding capsule is shown in Fig. 2*B*, *Inset* and measured RT dispersion curves for low-foot vs. high-foot drives are shown as growth factor vs. mode number in Fig. 2*B*.

The high-foot drive has a stronger leading shock, and three total shocks instead of four, to increase the entropy, decrease the shell and hot-spot compression and reduce the amount of shell mass mixing into the hot spot. This is done by reducing the steepness of the density profile (increasing the density gradient scale length) at the ablation front and the shell–hot-spot interfaces. Also, the stronger leading shock leads to favorable changes in the RM phase of instability growth due to the RM oscillations at the ablation front described earlier (36), albeit at a lower fuel and hot-spot areal density. We see in Fig. 2*B* that the peak in the ablation-front growth factor curves is at a Legendre mode number of 60–70 and there is an ablative cutoff at approximately mode 160. Very similar values are found in the simulation (solid curve) and the experiment (symbols with error bars). We observe an ablation-front RT peak growth factor of ∼1,000 for the low-foot drive vs. ∼200 for the high-foot drive. It is clear that the high-foot drive generates conditions that are more hydrodynamically stable, compared with the low-foot drive. The image in Fig. 2*B*, *Inset* shows an example inflight backlit X-ray radiograph of a capsule implosion with a preimposed perturbation with mode numbers of $l = 60$ (left-hand side) and 90 (right-hand side), near peak growth for the low-foot drive, and the raw data lineout is shown in Fig. 2*B*, *Bottom* (35, 39).

Profiles of density and temperature vs. radius at bang time from simulations are shown in Fig. 2*C* for the low-foot (low-adiabat) drive (17). Fig. 2*C*, *Inset* shows the capsule configuration. This 20-ns drive was developed to minimize the entropy created by shock heating, thereby maximizing the peak compression for cryogenic layered DT implosions. For enhanced diagnostic access, surrogate implosions are performed with an extra layer of ablator material to replace the normally cryogenic DT fuel layer and filled with gas. The simulation results given in Fig. 2*C* show that the CH shell (initial density of 1 g/cm^3) has been compressed to nearly 150 g/cm^3, corresponding to an increase in density of over a factor of 100 (blue curve in Fig. 2*C*). The peak temperature in the hot-spot DT gas fuel in this simulation was 4 keV, which leads to the predicted nuclear burn profile of 14-MeV DT neutrons/cm^3 vs. radius shown by the gray curve in Fig. 2*C*.

To complete this sequence of experiments, we show in Fig. 2*D* the results from experiments to infer the amount of atomic mix ending up in the hot spot at peak burn from a smooth capsule without a preimposed perturbation on the outer surface. A deuterated layer of CD is put at or near the shell–hot-spot interface in the CH(Si) capsule, with a pure tritium (T_2) gas fill, as illustrated in Fig. 2*D*, *Inset*. If there is atomic mix from the CD layer in the shell into the T_2 hot spot, there will be DT nuclear reactions, generating 14-MeV neutrons. The experimental yield of these 14-MeV DT neutrons vs. the recession depth of the CD layer is plotted in Fig. 2*D*. We see the expected trend: As the recession depth of the CD layer is increased, the amount of DT yield (mix) decreases monotonically (43, 45). This allowed the extent of original shell material that mixed into the hot spot by peak compression (bang time) to be determined, giving a mix width value of $h_{mix} \approx 2$–3 μm. Using the same methodologies validated in HGR experiments, detailed modeling of cryogenic layered, DT implosions on the NIF, such as those shown in Fig. 1 *A* and *B* and described in ref. 13, approximately match the measured integrated implosion observables (neutron yield, total compression, hot-spot temperature, and ablator–hot-spot mixing). These simulations used the measured capsule surface roughness and account for other known perturbation sources, such as the support tent, fill tube, and hohlraum drive asymmetries.

Embedded Interface, Planar Hydrodynamic Instability Experiments

We also developed and carried out a series of planar experiments in HED plasmas where a RT unstable region was formed at an embedded interface, which would not be significantly affected by the stabilizing effects of ablation, viscosity, or material strength. The experimental configuration is shown in Fig. 3*A*, where half of the NIF beams enter a hollow Au radiation cavity (hohlraum) and convert to a $T_R \sim 190$ eV radiation drive of 5–7 ns duration which ablatively accelerates the sample under study. The planar physics package that is accelerated is shown in Fig. 3*B*. It consists of a CH(3%I) ablator that is glued to an undoped polyamide–imide (PAI) layer, which is approximately transparent to the 9.0-keV Zn He-α backlighter X-rays used to radiograph the evolving interface from a side-on view. On the back side of the PAI layer, a square cross-section "trench" is machined into the PAI, and a CH(I) sample is precision fitted into this trench. Hence the front (driven side) and back sides of the physics package have CH(I) regions which are optically opaque, whereas the

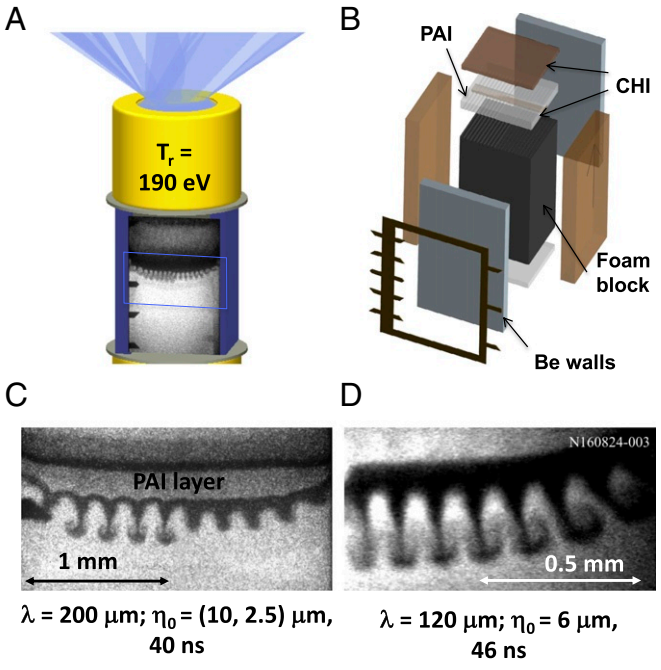

Fig. 3. Results of inflight radiography experiments in planar geometry on the NIF (44). (*A*) The experimental configuration for this NIF experiment, showing the hohlraum radiation cavity on the top and experimental package mounted off the end of the hohlraum on the bottom. (*B*) Sketch of the target components and assembly of the physics package, corresponding to the plastic ablator layers and foam tamper section. (*C*) Side-on flash X-ray radiograph at 40 ns after the NIF drive laser turned on, for NIF shot N160105-002 showing an unstable interface with a perturbation of wavelength of 200 μm for two different initial amplitudes (η_0 = 10.0 μm on the left and 2.5 μm on the right). (*D*) At later time (46 ns) on a separate shot, a side-on flash X-ray radiograph of the RT bubble and spike front development, showing signs of entering the advanced stages of RT evolution, for a wavelength of 120 μm and initial amplitude perturbation of 6 μm. Reproduced from ref. 44, with permission of AIP Publishing.

middle part of the target is undoped polyamide–imide, which is nearly transparent to the high-energy backlighter X-rays. This allows the side-on radiography experiments to measure 1D compression and decompression, which are needed to interpret the 2D side-on radiographs, so that the simple "accordion-like" 1D decompression is not mistaken for RT growth.

When the laser drive turned off, this physics package then decelerated for tens of nanoseconds, during which time the plastic-foam rippled interface was RT unstable. The resulting RT growth was measured at 40 ns after the laser drive turned on, with pulsed, side-on X-ray radiography. The radiograph in Fig. 3*C* shows the RT growth, including the spike tip formation at 40 ns from a $\lambda = 200$ μm perturbation with two different initial amplitudes, $\eta_0 = 2.5$ μm and 10 μm. Later in time at 46 ns, for a $\lambda = 120$ μm, $\eta_0 = 6$ μm perturbation, the data exhibit the beginning stages of a transition to the advanced stages of RT evolution, showing the RT bubble and spike shape and spike tip Kelvin–Helmholtz roll-ups, as illustrated in Fig. 3*D* (44, 49).

Radiative Shock Stabilization of Planar Hydrodynamic Instabilities

Fig. 4 shows a planar, RT experimental design whereby a strong shock is launched into a doped plastic ablator of density 1.4 g/cm^3 and then enters a low-density 0.2 g/cm^3 SiO_2 aerogel foam tamper region of the target, where the shock becomes radiative (Fig. 4*A*). This creates a strong source of radiation from the radiative shock in the SiO_2 foam which can reduce the perturbation growth at the plastic–foam interface by ablative stabilization (52–54). A radiation cavity (hohlraum, 4 mm diameter × 3 mm long, shown in Fig. 4*A*, *Left*) converts the blue light from the NIF laser to a soft X-ray source of radiation at temperatures ranging from 200 eV to 350 eV (as shown in Fig. 4*B*), which in turn ablatively launches a strong shock into the CH ablator. Note that the peak in the radiation drive occurs during peak laser intensity around 3–5 ns, but the radiation does not immediately drop to zero when the optical laser turns off around 5 ns. There is a radiation afterglow that continues for 20 ns or longer.

In Fig. 4*C*, we show the 2D radiation-hydrodynamics simulations (55) of the perturbation growth at the RT unstable polyimide (PI)–foam interface, as a function of the hohlraum drive strength ranging from $T_R \sim 200$ eV to 350 eV. These 2D simulations assume a preimposed single-mode sinusoidal perturbation at the PAI–foam interface of wavelength $\lambda = 120$ μm and amplitude $\eta_0 = 6$ μm. Interestingly, the RT growth for the high-hohlraum drive cases is lower than that for the low-drive simulations. Analysis of these 2D simulations shows that the shock in the SiO_2 foam for the high-drive simulations is sufficiently hot and radiative that this radiation and heat conduction ablatively stabilizes the RT growth at the PI–foam interface. Conversely, for the low-drive case, the resulting shock in the foam is not sufficiently radiative and the shocked foam is not hot enough to stabilize the RT growth. Hence, the predicted RT growth is close to classical and, at the same interface distance traveled, is 40% larger than that of the high-drive case. Preliminary experiments on the NIF laser are shown in Fig. 4*D* and exhibit a similar effect (54). In both the simulations and experiments, the mix width increases monotonically with time, as expected from basic instability theory (56–58). Quantitative dependence of the growth rate of RT instability on radiation temperature and spectrum is a challenging problem worthy of additional investigation.

Material Strength Stabilized Hydrodynamic Instability Experiments

Finally, we describe a set of planar experiments on the NIF where the ductile metal sample under study is taken to high pressure but kept in the solid state. A variety of materials are being studied on the NIF in this effort; we discuss the tantalum (Ta) experiments here (59). To reach high pressure but keep the physics package solid requires a ramped compression wave, low-adiabat drive that can maintain an acceleration for many tens of nanoseconds. One approach to generating such a ramped drive is a reservoir–gap–sample configuration developed by Barnes et al. (60) in the 1970s and adapted to our HED laser experiments as shown in Fig. 5*A* (61). A strong shock is launched through a plastic "reservoir," which in this experiment is a planar CH ablator attached over a window (hole) in the side of the hohlraum wall. The X-ray radiation from the hohlraum launches a strong shock through the plastic reservoir. When the shock breaks out the back side of the reservoir, the resulting releasing plasma sweeps across a vacuum

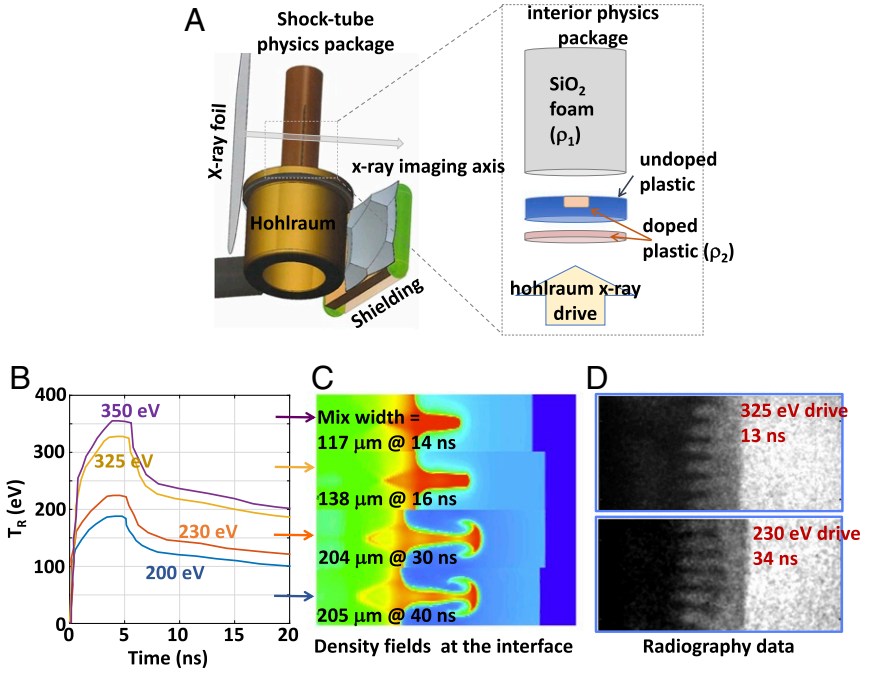

Fig. 4. Radiative shock experiments on the NIF (54). (*A*) The experimental configuration of this NIF experiment showing the overall setup (*Left*) and the components of the physics package (*Right*). (*B*) Simulated radiation temperature T_R (eV) vs. time (ns) for four NIF experiments, corresponding to peak radiation temperatures (top to bottom) of 350 eV, 325 eV, 230 eV, and 200 eV. (*C*) The corresponding 2D simulation results of the perturbation growth due to the RT instability for a preimposed ripple of wavelength of 120 μm and an amplitude of 6 μm, for roughly the same interface distance traveled. The color scale represents density (arbitrary units). (*D*) Experimental radiography data for the $T_R \sim 325$-eV drive at 13 ns (*Top*) and for $T_R \sim 230$ eV at 34-ns delay times (*Bottom*). The suppression of the ripple growth for the high-T_R drive is clearly observed, showing the effect of heat conduction stabilization of the RT instability; namely, the observed RT growth is reduced from classical, as described in the main text.

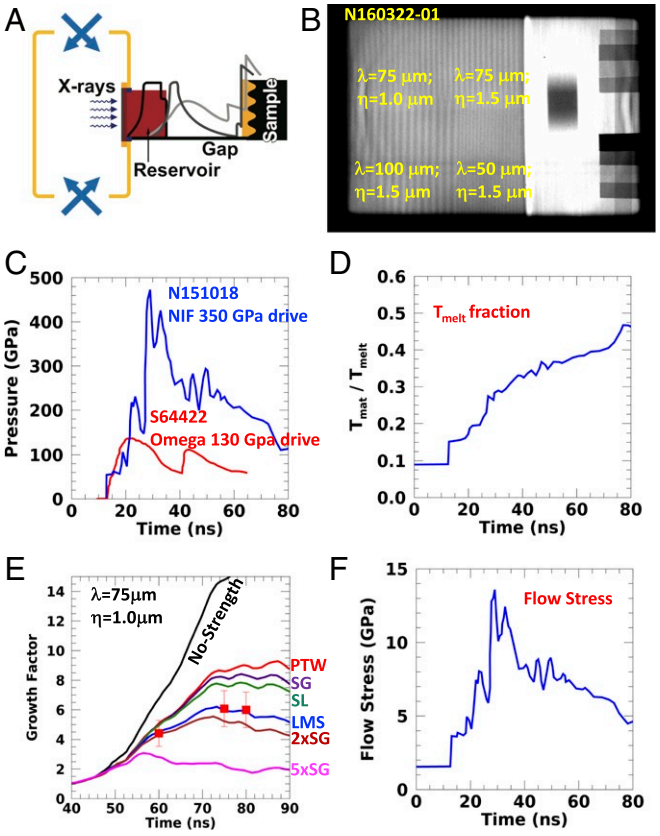

Fig. 5. Results from high-pressure, solid-state material dynamics experiments on the NIF. (*A*) The experimental configuration of this NIF experiment (not to scale) showing the reservoir–gap–sample configuration, which creates a ramp compression wave for the physics package mounted on the side of the hohlraum that takes it to high pressure, but keeps it in the solid state. (*B*) A face-on radiography image showing the late time perturbation growth for the experiment shown in *A*. (*C*) Simulated pressure vs. time in the Ta physics sample for the NIF (blue curve) and Omega (red curve) experiments. (*D*) The simulated material temperature divided by the melt temperature vs. time (nanoseconds) in the Ta sample. (*E*) Experimentally measured (red symbols) perturbation growth factors vs. time (nanoseconds) for the $P_{max} \sim$ 350 GPa NIF strength experiments. Simulations using different strength models are shown: from the top down, no strength (black curve), PTW [red (62)], SG [purple (63)], SL [green (64)], LMS [blue (65)], 2×SG (dark red curve), and 5×SG (pink curve). (*F*) The simulated strength (flow stress, in gigapascals) in the Ta physics sample, using the drive that was tuned to reproduce the experimentally measured sample pressure vs. time and using the LMS strength model.

gap and stagnates on the heat shield (thin CH layer) glued onto the rippled Ta physics package. This drive accelerates the sample (physics package), while keeping it at high pressure and in the solid state. An example time-resolved radiograph for Ta at late time, t = 60 ns, is shown in Fig. 5*B*. The corresponding pressure vs. time on the sample, P(t), is shown in Fig. 5*C*, with $P_{max} \sim$ 350 GPa. Note that the sample is at pressure and accelerating for $> \sim$30 ns. Fig. 5*D* shows $T_{sample} \ll T_{melt}$ vs. time from the simulations, which predict that the physics sample remains more than a factor of 2 below the melt curve for the useful duration of the experiment.

The interface between the stagnating plasma reservoir and the rippled Ta payload is RT unstable during this acceleration. Preimposed ripples in the Ta tend to grow due to the RT instability, but the rate of growth is reduced by the high-pressure (100–500 GPa), high-strain rate (10^6–10^7 s^{-1}) material strength of the solid-state Ta. The sensitivity of the RT growth factors to the material strength stabilization is shown in Fig. 5*E* for peak pressure of 350 GPa and for different strength models: Preston–Tonks–Wallace (PTW) (62), Steinberg–Guinan (SG) (63), Steinberg–Lund (SL) (64), LLNL multiscale (LMS) (65), SG multiplied by a factor of 2 at all conditions and all times (2×SG), and SG multiplied by a factor of 5 (5×SG).

One of the simplest strength models is the SG model (63), where the material strength, σ, of the sample increases with pressure and strain (ϵ) decreases with temperature and is independent of strain rate,

$$\sigma_{SG} = \sigma_0 f(\epsilon)[G(P, T)/G_0] \quad [2]$$

and

$$G(P, T) = G_0 \left[1 + \frac{G'_P}{G_0}\frac{P}{\eta^{1/3}} + \frac{G'_T}{G_0}(T - 300)\right], \quad [3]$$

where G is the material shear modulus; $G'_P = dG/dP$; $G'_T = dG/dT$; $\eta = \rho/\rho_0$ = compression; and $f(\epsilon) = [1 + b(\epsilon_i + \epsilon)]^n$ is the work hardening factor as a function of plastic strain ϵ and any initial strain, ϵ_i, before the start of the dynamic experiment. Inspection of Eqs. **2** and **3** suggests that solids can become very strong at high pressure.

The PTW model (62) is a more sophisticated strength model which includes strain rates and has been applied favorably to experiments at the high strain rates of laser experiments (66). The LMS strength model adds yet another level of sophistication, by tying the components of the model to ab initio theory and direct numerical simulations, based on quantum-based interatomic potentials and dislocation mobilities (65). The Steinberg-Lund, PTW, and LMS models all predict that strength increases monotonically with strain rate. The net result of our laser experiments at high pressures and strain rates is that the Ta sample is predicted to be very strong, as shown in Fig. 5*F*, based on the LMS model, which reproduces reasonably well the RT experimental results shown in Fig. 5*E*. The inferred peak flow stress (strength) of the Ta physics sample is ~10 GPa at $P_{max} \sim$ 350 GPa, and $d\epsilon/dt \sim 10^7$ s^{-1}, while keeping the sample solid, $T_{sample} < T_{melt}$. These strength levels (flow stress) at this extreme condition are large and it remains to be explored in future experiments whether the strength continues to rise monotonically with increasing pressure.

Conclusion

We developed experiments on the NIF to study the RT instability and advanced stages of RT evolution at a wide variety of extreme conditions, from hot, dense plasmas and burning hot spots to relatively cool, high-pressure materials undergoing solid-state, plastic flow at high strain and strain rate. We carried out experiments in HED regimes at an ablation front and at an embedded interface with or without the presence of a strongly radiative shock. These experiments were conducted in either planar or spherical geometry. HED conditions with and without strong radiative effects were shown. The solid-state plastic flow experiments shown in Fig. 5 allow us to study material response at pressures of 100–500 GPa and high strain rates, 10^6–10^8 s^{-1}. We found that the material strength in these-high pressure, high-strain rate plastic flow experiments is large and can significantly reduce the RT growth rates compared with classical values. For these high-pressure, high-strain rate, short-timescale conditions, there seems to be little sensitivity to sample initial microstructure. These results are relevant to planetary formation dynamics at high pressures (67). We find that widely used models for high-pressure strength differ significantly from one another at these extreme conditions of solid-state plastic flow. An intriguing consideration is the possibility of using these findings to enhance resistance to hydrodynamic instabilities in advanced designs of ICF capsule implosions.

ACKNOWLEDGMENTS. We gratefully acknowledge the insightful discussions and input from Dr. Stephen MacLaren from LLNL in the early stages of preparing this manuscript. And we appreciate the critical reading and useful suggestions of the referees. This work was performed under the auspices of the US Department of Energy by LLNL under Contract DE-AC52-07NA27344. We gratefully acknowledge the access to the NIF facility for the basic science experiments described in several of the figures, which was through the NIF Discovery Science program, which issues an annual call for proposals for basic science experiments on NIF.

1. Drake R (2005) Hydrodynamic instabilities in astrophysics and in laboratory high-energy-density systems. *Plasma Phys Controlled Fusion* 47:B419–B440.
2. Dahl TW, Stevenson DJ (2010) Turbulent mixing of metal and silicate during planet accretion–And interpretation of the Hf-W chronometer. *Earth Planet Sci Lett* 295:177–186.
3. Nellis W, Ross M, Holmes N (1995) Temperature-measurements of shock-compressed liquid-hydrogen–Implications for the interior of Jupiter. *Science* 269:1249–1252.
4. Seager S, Kuchner M, Hier-Majumder CA, Militzer B (2007) Mass-radius relationships for solid exoplanets. *Astrophys J* 669:1279–1297.
5. Pahlevan K, Stevenson DJ (2007) Equilibration in the aftermath of the lunar-forming giant impact. *Earth Planet Sci Lett* 262:438–449.
6. Lock SJ, Stewart ST (2017) The structure of terrestrial bodies: Impact heating, corotation limits, and synestias. *J Geophys Res Planets* 122:950–982.
7. Arnett W, Bahcall J, Kirshner R, Woosley S (1989) Supernova 1987A. *Annu Rev Astron Astrophys* 27:629–700.
8. Woosley S, Weaver T (1995) The evolution and explosion of massive stars. II. Explosive hydrodynamics and nucleosynthesis. *Astrophys J Suppl Ser* 101:181–235.
9. Barthelmy S, et al. (2005) An origin for short gamma-ray bursts unassociated with current star formation. *Nature* 438:994–996.
10. van Weeren RJ, Rottgering HJA, Brueggen M, Hoeft M (2010) Particle acceleration on megaparsec scales in a merging galaxy cluster. *Science* 330:347–349.
11. Lindl J, et al. (2004) The physics basis for ignition using indirect-drive targets on the National Ignition Facility. *Phys Plasmas* 11:339–491.
12. Edwards MJ, et al. (2013) Progress towards ignition on the National Ignition Facility. *Phys Plasmas* 20:070501.
13. Clark DS, et al. (2016) Three-dimensional simulations of low foot and high foot implosion experiments on the National Ignition Facility. *Phys Plasmas* 23:056302.
14. Spaeth ML, et al. (2016) Description of the NIF laser. *Fusion Sci Technol* 69:25–145.
15. Haynam CA, et al. (2007) National Ignition Facility laser performance status. *Appl Opt* 46:3276–3303.
16. Boehly T, et al. (1997) Initial performance results of the OMEGA laser system. *Opt Commun* 133:495–506.
17. Ma T, et al. (2017) The role of hot spot mix in the low-foot and high-foot implosions on the NIF. *Phys Plasmas* 24:056311.
18. Bodner S (1974) Rayleigh-Taylor instability and laser-Pellet fusion. *Phys Rev Lett* 33:761–764.
19. Munro D (1988) Analytic solutions for Rayleigh-Taylor growth-rates in smooth density gradients. *Phys Rev A* 38:1433–1445.
20. Takabe H, Mima K, Montierth L, Morse R (1985) Self-consistent growth-rate of the Rayleigh-Taylor instability in an ablatively accelerating plasma. *Phys Fluid* 28:3676–3681.
21. Kull H (1986) Nonlinear free-surface Rayleigh-Taylor instability. *Phys Rev A* 33:1957–1967.
22. Sanz J (1994) Self-consistent analytical model of the Rayleigh-Taylor instability in inertial confinement fusion. *Phys Rev Lett* 73:2700–2703.
23. Betti R, Goncharov V, McCrory R, Verdon C (1995) Self-consistent cutoff wave-number of the ablative Rayleigh-Taylor instability. *Phys Plasmas* 2:3844–3851.
24. Goncharov V, Betti R, McCrory R, Sorotokin P, Verdon C (1996) Self-consistent stability analysis of ablation fronts with large Froude numbers. *Phys Plasmas* 3:1402–1414.
25. Goncharov V, Betti R, McCrory R, Verdon C (1996) Self-consistent stability analysis of ablation fronts with small Froude numbers. *Phys Plasmas* 3:4665–4676.
26. Jacobs J, Catton I (1988) 3-Dimensional Rayleigh-Taylor instability 1. Weakly nonlinear-theory. *J Fluid Mech* 187:329–352.
27. Jacobs J, Catton I (1988) 3-Dimensional Rayleigh-Taylor instability 2. Experiment. *J Fluid Mech* 187:353–371.
28. Anisimov SI, Drake RP, Gauthier S, Meshkov EE, Abarzhi SI (2013) What is certain and what is not so certain in our knowledge of Rayleigh-Taylor mixing? *Philos Trans R Soc A Math Phys Eng Sci* 371:20130266.
29. Meshkov E (2013) Some peculiar features of hydrodynamic instability development. *Philos Trans R Soc A Math Phys Eng Sci* 371:20130267.
30. Abarzhi SI (2010) Review of theoretical modelling approaches of Rayleigh-Taylor instabilities and turbulent mixing. *Philos Trans R Soc A Math Phys Eng Sci* 368:1809–1828.
31. Azechi H, et al. (2007) Comprehensive diagnosis of growth rates of the ablative Rayleigh-Taylor instability. *Phys Rev Lett* 98:045002.
32. Aglitskiy Y, et al. (2010) Basic hydrodynamics of Richtmyer-Meshkov-type growth and oscillations in the inertial confinement fusion-relevant conditions. *Philos Trans R Soc A Math Phys Eng Sci* 368:1739.
33. Hurricane OA, et al. (2014) The high-foot implosion campaign on the National Ignition Facility. *Phys Plasmas* 21:056314.
34. Regan SP, et al. (2013) Hot-spot mix in ignition-scale inertial confinement fusion targets. *Phys Rev Lett* 111:045001.
35. Casey DT, et al. (2014) Reduced instability growth with high-adiabat high-foot implosions at the National Ignition Facility. *Phys Rev E* 90:011102.
36. MacPhee AG, et al. (2015) Stabilization of high-compression, indirect-drive inertial confinement fusion implosions using a 4-shock adiabat-shaped drive. *Phys Plasmas* 22:080702.
37. Smalyuk VA, et al. (2017) Mix and hydrodynamic instabilities on NIF. *J Instrum* 12:C06001.
38. Park HS, et al. (2014) High-adiabat high-foot inertial confinement fusion implosion experiments on the National Ignition Facility. *Phys Rev Lett* 112:055001.
39. Peterson JL, et al. (2015) Validating hydrodynamic growth in National Ignition Facility implosions. *Phys Plasmas* 22:056309.
40. Pickworth LA, et al. (2016) Measurement of hydrodynamic growth near peak velocity in an inertial confinement fusion capsule implosion using a self-radiography technique. *Phys Rev Lett* 117:035001.
41. Weber CR, et al. (2016) First measurements of fuel-ablator interface instability growth in inertial confinement fusion implosions on the National Ignition Facility. *Phys Rev Lett* 117:075002, and erratum (2016) 117:159902.
42. MacPhee AG, et al. (2017) X-ray shadow imprint of hydrodynamic instabilities on the surface of inertial confinement fusion capsules by the fuel fill tube. *Phys Rev E* 95:069905.
43. Casey DT, et al. (2014) Development of the CD Symcap platform to study gas-shell mix in implosions at the National Ignition Facility. *Phys Plasmas* 21:092705.
44. Nagel SR, et al. (2017) A platform for studying the Rayleigh-Taylor and Richtmyer-Meshkov instabilities in a planar geometry at high energy density at the National Ignition Facility. *Phys Plasmas* 24:072704.
45. Smalyuk VA, et al. (2014) Measurements of an ablator-gas atomic mix in indirectly driven implosions at the National Ignition Facility. *Phys Rev Lett* 112:025002.
46. Smalyuk VA, et al. (2014) First measurements of hydrodynamic instability growth in indirectly driven implosions at ignition-relevant conditions on the National Ignition Facility. *Phys Rev Lett* 112:185003.
47. Raman KS, et al. (2014) An in-flight radiography platform to measure hydrodynamic instability growth in inertial confinement fusion capsules at the National Ignition Facility. *Phys Plasmas* 21:072710.
48. Weber CR, et al. (2017) Improving ICF implosion performance with alternative capsule supports. *Phys Plasmas* 24:056302.
49. Wang P, et al. (2017) Three-dimensional design simulations of a high-energy density reshock experiment at the National Ignition Facility. *J Fluids Eng* 140:41207–41210.
50. Casey DT, et al. (2015) Improved performance of high areal density indirect drive implosions at the National Ignition Facility using a four-shock adiabat shaped drive. *Phys Rev Lett* 115:105001.
51. Smalyuk VA, et al. (2016) Experimental results of radiation-driven, layered deuterium-tritium implosions with adiabat-shaped drives at the National Ignition Facility. *Phys Plasmas* 23:102703.
52. Huntington CM, et al. (2011) Design of experiments to observe radiation stabilized Rayleigh-Taylor instability growth at an embedded decelerating interface. *Phys Plasmas* 18:112703.
53. Kuranz CC, et al. (2011) Astrophysically relevant radiation hydrodynamics experiment at the National Ignition Facility. *Astrophys Space Sci* 336:207–211.
54. Kuranz CC, et al. (2018) How high energy fluxes may affect Rayleigh-Taylor instability growth in young supernova remnants. *Nat Commun* 9:1564.
55. Darlington R, McAbee T, Rodrigue G (2002) Large eddy simulation and ALE mesh motion in Rayleigh-Taylor instability simulation. *Comput Phys Commun* 144:261–276.
56. Haan S (1989) Onset of nonlinear saturation for Rayleigh-Taylor growth in the presence of a full spectrum of modes. *Phys Rev A* 39:5812–5825.
57. Haan S (1991) Weakly nonlinear hydrodynamic instabilities in inertial fusion. *Phys Fluids B Plasma Phys* 3:2349–2355.
58. Malamud G, et al. (2014) Reshocked Richtmyer-Meshkov instability: Numerical study and modeling of random multi-mode experiments. *Phys Fluid* 26:084107.
59. Park HS, et al. (2015) Grain-size-independent plastic flow at ultrahigh pressures and strain rates. *Phys Rev Lett* 114:065502.
60. Barnes J, Blewett P, Mcqueen R, Meyer K, Venable D (1974) Taylor instability in solids. *J Appl Phys* 45:727–732.
61. Prisbrey ST, et al. (2012) Tailored ramp-loading via shock release of stepped-density reservoirs. *Phys Plasmas* 19:056311.
62. Preston D, Tonks D, Wallace D (2003) Model of plastic deformation for extreme loading conditions. *J Appl Phys* 93:211–220.
63. Steinberg D, Cochran S, Guinan M (1980) A constitutive model for metals applicable at high-strain rate. *J Appl Phys* 51:1498–1504.
64. Steinberg D, Lund C (1989) A constitutive model for strain rates from 10^{-4} to 10^{6} s^{-1}. *J Appl Phys* 65:1528–1533.
65. Barton NR, et al. (2011) A multiscale strength model for extreme loading conditions. *J Appl Phys* 109:073501.
66. Remington B, et al. (2006) Material dynamics under extreme conditions of pressure and strain rate. *Mater Sci Technol* 22:474–488.
67. Stevenson D (2003) Mission to Earth's core–A modest proposal. *Nature* 423:239–240.